



Advanced Water Management in PEFCs: Diffusion Layers with Patterned Wettability

II. Measurement of Capillary Pressure Characteristic with Neutron and Synchrotron Imaging

A. Forner-Cuenca,^{a,*} J. Biesdorf,^a A. Lamibrac,^a V. Manzi-Orezzoli,^a F. N. Büchi,^a L. Gubler,^{a,**} T. J. Schmidt,^{a,b,**} and P. Boillat^{a,c,**,z}

^aElectrochemistry Laboratory, Paul Scherrer Institut, 5232 Villigen PSI, Switzerland

^bLaboratory of Physical Chemistry, Department of Chemistry & Applied Biosciences, ETH Zürich, 8093 Zürich, Switzerland

^cNeutron Imaging and Activation Group, Paul Scherrer Institut, 5232 Villigen PSI, Switzerland

In this paper, we present an experimental study on the development of gas diffusion layer (GDL) materials for fuel cells with dedicated water removal pathways generated using radiation induced grafting of hydrophilic compounds onto the hydrophobic polymer coating. The impact of several material parameters was studied: the carbon substrate type, the coating load, the grafted chemical compound and the pattern design (width and separation of the hydrophilic pathways). The corresponding materials were characterized for their capillary pressure characteristic during water imbibition experiments, in which we also evidenced the differences between injection from a narrow distribution channel in the center of the material (and thus strongly relying on lateral transport) and homogeneous injection from one face of the material. All materials parameters were observed to have a significant influence on the water distribution. In particular, the type of substrate has a dramatic impact, with results ranging from a nearly perfect separation of water between hydrophilic and hydrophobic domains for substrates having a narrow pore size distribution to a fully random imbibition of the material for substrates having a broad pore size distribution.

© The Author(s) 2016. Published by ECS. This is an open access article distributed under the terms of the Creative Commons Attribution Non-Commercial No Derivatives 4.0 License (CC BY-NC-ND, <http://creativecommons.org/licenses/by-nc-nd/4.0/>), which permits non-commercial reuse, distribution, and reproduction in any medium, provided the original work is not changed in any way and is properly cited. For permission for commercial reuse, please email: oa@electrochem.org. [DOI: 10.1149/2.0511609jes] All rights reserved.

Manuscript submitted May 3, 2016; revised manuscript received June 24, 2016. Published July 7, 2016.

Research is striving to increase power density of polymer electrolyte fuel cells (PEFCs). Improving the catalytic activity and optimizing the water management are frequently identified as key approaches for maximizing power density or reducing the cost.^{1–4} The gas diffusion media (GDM), which are located between electrodes and flow fields, affect the complex water management in PEFCs to a significant extent. GDMs, generally composed by an arrangement of a gas diffusion layer (GDL) and a microporous layer (MPL), simultaneously provide several functionalities. They conduct electrons and heat, maintain the mechanical integrity of the membrane electrode assembly and should maximize gas diffusivity while removing the liquid water toward the flow field channels.^{5–7} Oxygen diffusivity exponentially decreases as saturation of pores with water increases.^{8,9} This is related to the blocking of available pores and a concomitant increase of tortuosity for liquid and gas transport counterflow. Focusing on the GDL, researchers have tried to optimize gas-liquid transport characteristics by finding optimal coating loads,^{10–14} understanding the effects of microstructure,^{15–18} developing novel coatings^{19–22} and using different architectures or substrates.^{23,24} A clever way for improving the gas-liquid transport consists of artificially creating pathways within the GDL for effective water removal and thereby increasing the gas diffusivity. In this direction, improvements under certain operating conditions were measured using perforated GDLs^{25–27} and enhanced oxygen diffusivities were achieved using a locally coated GDL.²⁸ Recently, we reported a method to produce GDLs with patterned wettability based on local modifications of the polymer coating's wettability using radiation grafting.^{29,30} Contrary to the other approaches, the radiation grafting method allows wettability modifications across the complete material thickness without altering the mechanical properties and, most importantly, it offers realistic scale-up potential. Here, we present a detailed experimental study on the ability of our newly proposed material to confine the liquid water transport to predefined pathways. This study was realized by varying

different material parameters (type of carbon substrate, coating load, type of grafted compound, geometry of the water pathways). The materials were characterized by the recording of local water saturation as a function of capillary pressure in water injection experiments, where the water distribution was obtained by neutron radiography for all samples, and additionally by X-ray tomographic microscopy (XTM) for one selected sample.

Experimental

Materials preparation.—Toray TGP-H-060 carbon paper (~190 μm thickness and 78% porosity) was obtained from Fuel Cell Earth (Woburn, Massachusetts).³¹ Sigracet GDL 24 AA (~190 μm thickness and 86% porosity) was purchased at Ion Power (New Castle, Delaware).³² Freudenberg H2315 –H23/H24 current designation—(~210 μm thickness) was obtained from QuinTech (Goeppingen, Germany).³³

All three types of gas diffusion layers were obtained in pristine condition (uncoated). The pristine GDLs were coated in-house with fluorinated ethylene propylene (FEP). FEP was chosen over tetrafluoroethylene (PTFE) due to its superior radiation resistance, faster grafting kinetics and superior hydrophobicity. A standard dip-coating procedure using water dispersions of FEP particles and a subsequent thermal treatment was followed, which is described in our previous work.^{29,34} Coating loads of 5, 30 and 70%wt were targeted (Table I). Calibration curves, relating the FEP concentration in the dispersion to the final coating load, were obtained for the different GDL substrates (Figure S1).

Samples were irradiated using an electron beam in an EBLab 200 sealed laboratory emitter system from Comet AG (Flamatt, Switzerland). The details were described in our previous work.²⁹ An acceleration voltage of 200 kV and a dose of 50 kGy were selected in each case. In order to create patterned materials, radiation-blocking masks were used. The masks' body is a 2 mm thick steel plate containing a regular arrangement of slits where the opening width coincides with the desired hydrophilic pattern width and the spacing between two slits corresponds to the hydrophobic pattern width. The different pattern

*Electrochemical Society Student Member.

**Electrochemical Society Member.

^zE-mail: pierre.boillat@psi.ch

Table I. Overview of samples used in the study.

Substrate type	FEP coating load [%wt]	Chemistry	Hydrophilic-hydrophobic width [μm – μm]
Toray	5	FEP-g-pNVF	500–930
	30	FEP-g-pNVF	500–930
	30	FEP-g-pAA	500–930
	30	-	-
	70	FEP-g-pNVF [#]	500–930
	70	FEP-g-pNVF	250–460
	70	FEP-g-pNVF	100–500
	70	FEP-g-pNVF*	100–100
SGL	70	-	-
	30	FEP-g-pNVF	500–930
	30	-	-
	70	FEP-g-pNVF*	250–460
Freudenberg	30	FEP-g-pNVF	500–930
	30	-	-
	70	FEP-g-pNVF	100–500

*The characterization of these samples is only presented in Supplementary Inf.

[#]Sample used for comparison (measured with both setups, NR and XTM).

designs are described in Table I. Masks with a slit width of 250 μm (or higher) were produced using a water jet (Waterjet AG, Aarwangen, Switzerland). For the realization of the narrowest designs (slits with a width of 100 μm), a combined water and laser cutting technique was employed (Laser MicroJet, Synova, Ecublens, Switzerland). After irradiation, samples were rapidly stored at -80°C to reduce radical recombination prior to grafting.

N-vinylformamide (NVF) was used as received (Sigma Aldrich 98%) without dilution. The irradiated GDLs were placed in cylindrical glass reactors, through which nitrogen was bubbled for 60 min to remove dissolved oxygen. After that, reactors were placed in a water bath at 70°C for 60 minutes. Acrylic acid (AA) was used as received (Sigma Aldrich 99%) and diluted (15% wt) in water. A vacuum reaction system allowed for deoxygenation and application of 50 mbar_{abs} pressure, which was needed in order to fill the hydrophobic pores and remove the trapped air. The setup and experimental procedure is described in detail in Ref. 34. Reactions with AA were performed at 60°C for 60 minutes.

The cleaning procedure was found to be critical for the effective formation of the wettability patterns. Samples were placed in a Buchner type filter and vacuum was applied in the vessel underneath. This helps the cleaning solvent to penetrate into the inner porosity with a convective flow. 300 mL of ethanol, 300 mL of isopropanol and finally 300 mL of water were used to clean each of the grafted materials in this manner.

Energy-dispersive X-ray (EDX) mapping and scanning electron microscopy (SEM).—The ion exchange from H^+ to Na^+ was performed only for characterization purposes and does not constitute a synthetic step. The sample treated with AA was exposed to 0.05 M NaOH overnight to form the sodium acrylate salt. The Na signal produced much higher contrast in the EDX maps compared to the O signal of the non-exchanged material.

The EDX mappings were recorded using a compatible accessory (EDX TSL, AMETEK) integrated into a scanning electron microscope FE-SEM Ultra 55 (Carl Zeiss, Oberkochen, Germany). They were taken with an acceleration voltage of 10 keV, an aperture of 60 μm and gun-to-sample distance of about 9 mm. Cross sections were prepared using an epoxy resin and subsequent polishing. The method is described elsewhere.^{20,35}

Method of standard porosimetry (MSP).—It is widely accepted that capillary pressure, P_c , is the driving force for liquid water transport within the GDLs.^{36,37} The method of standard porosimetry (MSP) consists of the measurement of the pore saturation, S , as a function of the capillary pressure and can be used with different wetting fluids.³⁸ Gostick et al. first adapted the method to porous gas diffusion layers for PEMFCs.³⁹ In their experimental setup the GDL sample was sandwiched between a hydrophilic and a hydrophobic membrane.⁴⁰ The hydrophobic membrane on top provides a very high pressure boundary which ensures the complete saturation of the GDL. In this configuration, the liquid distributor and the hydrophilic membrane beneath the sample ensures a homogeneously filled water front over the sample area. The former authors and other groups systematically obtained $P_c(S)$ relationships for different materials and studied the impact of substrate type, sample thickness, compression and sample wettability among other parameters.^{40–46} Recently, Lamibrac et al. developed a setup compatible with X-ray tomographic microscopy (XTM) imaging to perform MSP measurements.⁴⁷ Compared to previous attempts,^{48,49} the recent developments in terms of image processing and segmentation allowed extraction of quantitative $P_c(S)$ data from the XTM images.

In addition, in this work we adapted the previously described MSP method to inject water through a central distribution channel. In this case, the capillary pressure was controlled by regulating the liquid pressure by changing the water height. The water content was quantified using neutron radiography. A selected sample was characterized using the standard MSP setup with water over the complete bottom interface and the water distribution was imaged with XTM. All experiments were performed at room temperature.

Mono-channel injection setup.—In the present work, all samples where characterized using a setup in which the injection of water was done through a channel in the center of the cell which occupies 1/10 of the sample area. This modification was introduced for two reasons: first, if water would be injected all over the area the neutron radiographs performed in the *through-plane* direction would contain a superimposed water layer. With the new configuration, 90% of the sample area is free of extra water. Secondly, important information relating to “lateral transport”, i.e. transport in the GDL in-plane direction, can be extracted with this setup. Figure 1a shows the flow diagram of the setup used in all neutron radiography experiments. A water canister (30 L volume) was fixed on top of a precision motor (Berger Lahr VRDM 3913) and was connected to the main circuit (line a). The experimental sequence followed was: (I) valves V_1 and V_2 were switched to permit water flow through lines a-b-c to remove any gas bubbles present; (II) valves V_2 and V_3 were switched to permit flow through lines a-b-d-e. With the pressure sensor P_1 (at a fixed distance below the injection channel) the tank height could be adjusted adequately allowing water to flow at low overpressure (less than 1 mbar); (III) after the injection channel was completely filled (verified online with neutron imaging), V_3 was switched to dead-end mode where lines a-b-d were connected but without water flow; (IV) The capillary pressure, P_c , was calculated as $P_c = P_L - P_G$, where P_L is the pressure of the liquid water immediately before the cell inlet and at the same height as the injection channel and P_G is the gas pressure immediately after compartment 2. Each pressure setting was held for at least 5 minutes. The capillary pressure was varied only in increasing direction. Neutron radiographs and pressure data were acquired over the complete duration of the experiment; (V) after the data corresponding to the last capillary pressure point was acquired, compartment 1 was purged with N_2 and 1 NL/min was flown through both compartments (through lines f-b-d-e and g, respectively) in order to evaporate the water from the GDL in a controlled manner (between 3–6 minutes were required to fully evaporate the water at this flowrate) so that the water footprint in the GDL during evaporation could be imaged.

The cell configuration is depicted in Figure 1b. Compartment 1 contained the injection channel (1 mm width, 0.5 mm depth) in the center. A PTFE gasket of 350 μm was inserted and helped positioning the GDL. The GDL of interest (patterned GDL) was placed in

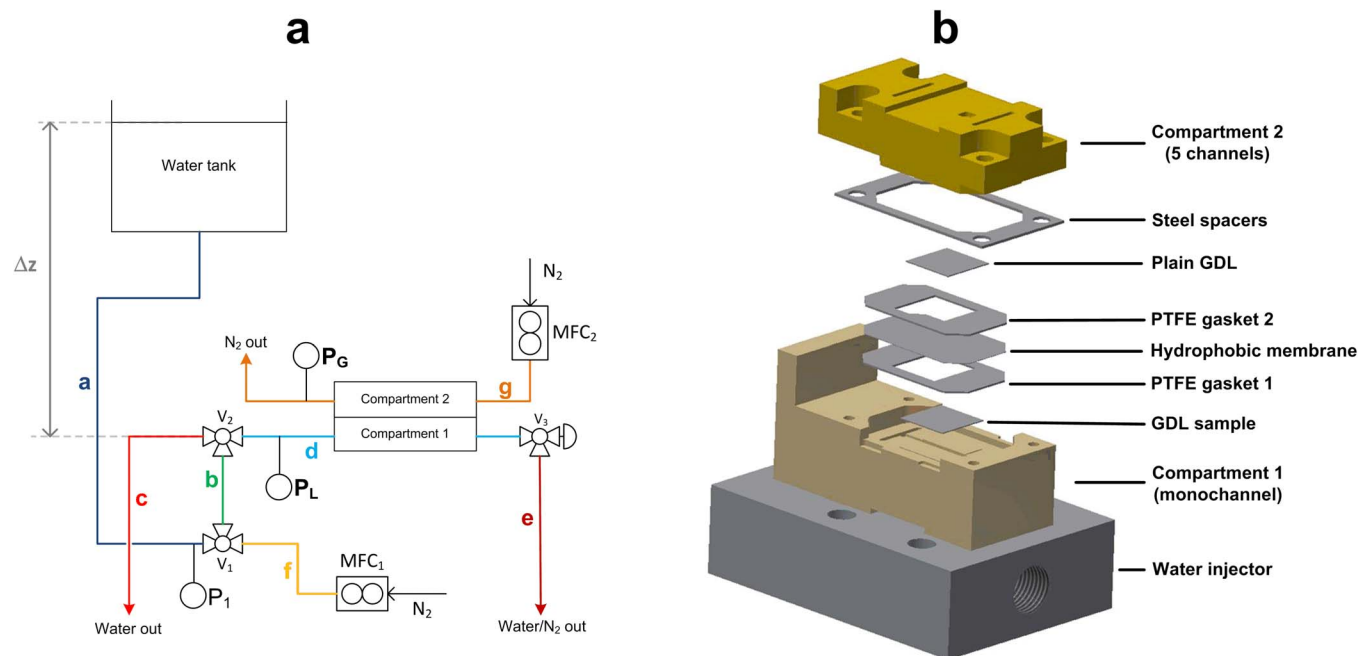


Figure 1. Experimental setup used in the capillary pressure experiments with neutron radiography. (a) Flow diagram of the experimental setup; (b) Cell detail showing the different elements. The GDL sample was oriented in parallel with the gravitational acceleration.

compartment 1 with the direction of the pattern perpendicular to the injection channel. On top, a hydrophobic membrane (HVHP04700, Durapore) of about 120 μm thickness was placed, followed by another PTFE gasket and another GDL (plain sample and of the same substrate as the GDL in compartment 1). The reason to use a second GDL is to mimic the compression conditions existing in an actual fuel cell. The use of steel spacers and the very same GDL substrate in both compartments allowed us to adjust the GDL compression to 20% in all the experiments.

Neutron radiography (NR).—Neutron radiography was performed at the ICON beam line of the SINQ spallation source at the Paul Scherrer Institute.⁵⁰ A 20 μm thick Gd_2O_3 scintillator screen mounted in the micro-setup detector including a CCD camera (Andoe DV436, 2048 \times 2048 pixels) was used for the recording of the neutron radiographs.⁵¹ The detector pixel pitch was 13.5 μm and the effective resolution 55 μm , taking into account the unsharpness due to the beam divergence. The exposure time was set to 30 s and the readout time was 4 s. All images underwent filtering for noise removal and image correction (subtraction of the detector background and of the scattered neutrons background, correction of the beam fluctuation and of the spatial inhomogeneities), after which they were divided by an image of the dry cell to obtain the attenuation due to water only.⁵² From the obtained transmission images, the quantitative water distribution was obtained by inversion of the Lambert-Beer law using a known attenuation coefficient of 4.5 cm^{-1} for this setup (calculated from Refs. 50,53).

Extraction of local capillary pressure – water thickness characteristics.—A study consisting of separately analyzing the water distribution above and below the injection channel showed no preferential water locations induced by height. Gravity does not seem to have a significant influence. Consequently, both domains (A_{above} and A_{below}) were considered when averaging attenuation (Figure 2a). Hydrophilic and hydrophobic patterns were analyzed independently. Averaging areas for the hydrophilic and hydrophobic lines were chosen as bands having half of the width of the corresponding region (see Figure 2b). Following this procedure, we extracted averaged attenuations (representative of the whole sample) for these areas and

converted them to a water thickness as described in the previous paragraph. In all NR experiments water thickness values are provided instead of saturation, because calculating the latter requires precise knowledge of the porosity and thickness of the compressed sample,

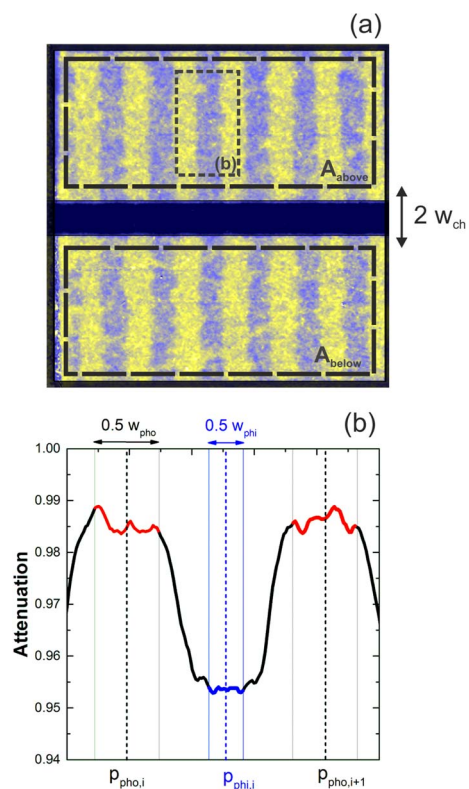


Figure 2. (a) Neutron radiograph showing the regions used for extracting the attenuation data. The GDL orientation (with respect to gravitational acceleration) is the same as shown in the radiograph; (b) Detail showing the averaging intervals for one hydrophilic domain and two hydrophobic domains.

which are difficult to estimate as a function of coating load, grafting treatment, and effective compression.

Homogeneous injection setup.—The experimental setup and procedure has been extensively described previously and was used identically in this work.⁴⁷ The GDL sample is sandwiched between two membranes: a hydrophilic membrane (pore size 0.22 μm) generates homogeneous injection of water from the bottom side, while a hydrophobic membrane on top confines the water and allows for saturations beyond the bubble point. Two consecutive cycles of imbibition (increasing P_C) and withdrawal (decreasing P_C) were performed, but only imbibition results are presented for the sake of clarity. X-ray tomographic microscopy (XTM) imaging was made at the TOMCAT beamline of the Swiss Light Source (SLS) with a beam energy of 13.5 keV. Tomographic scans with 2001 exposures of 10 ms were performed resulting in a scanning time of 20 s. The PCO edge camera and 2–4 \times zoom microscope system was used so images were obtained with a pixel/voxel size of 2.2 μm . More details on image processing, segmentation and derivation of the saturation vs. capillary pressure curves were extensively described by Lamibrac et al.⁴⁷ One sample (Toray 70%FEP-g-pNVF 500–930 μm , see Table I) was analyzed with this setup.

Results and Discussion

Resolution assessment of the grafted pattern.—Before presenting the results of the capillary pressure measurements on the modified materials, we show an ex-situ analysis of the obtained hydrophilic patterns. Figure 3a shows a regular optical image of a modified sample after immersing it in water. Water accumulates at the hydrophilic

patterns on both the top and bottom surface. A closer look with an optical microscope confirms the localization of water (Figure 3b). EDX mapping allows for identification of the grafted molecules' distribution. The carbon signal is mainly derived from carbon fibers and, to a lesser extent, the coating, while the fluorine signal originates from the FEP polymer (Figure 3c). The sodium signal comes exclusively from sodium polyacrylate salt formed during ion exchange in aqueous NaOH. The sodium mapping shows that grafted polyacrylic acid is located in a narrow space of about 100 μm width on the available coating surfaces (Toray 70%FEP-g-pAA 100–500 μm). Figure 3d shows the averaged Na-intensity from the EDX mapping from top and bottom surfaces of a modified sample. The top surface refers to the GDL surface directly exposed to the electron radiation. Despite the intrinsically irregular nature of the material, there is a fairly good agreement between both signals. The fact that the bottom surface (opposite to the irradiated surface) presents a similarly modified pattern suggests that the electron beam activation effectively occurs without significant detrimental scattering effects. In order to validate that grafting polymerization happens throughout the bulk of the material, electron microscopy of cross-sections (prepared via embedding in an epoxy resin) was performed (Figures 3e and 3f). The use of the secondary electron detectors showed notable contrast variations between original coating (FEP) and grafted copolymer (FEP-g-pAA). This distinction is probably due to the difference in electrical conductivity, as reported in previous works.^{34,54}

Variation of material parameters.—Figure 4 presents a collection of water thickness vs capillary pressure curves for the most relevant materials. The graphs have been organized in the following fashion: in vertical alignment (Figures 4a, 4d and 4f) three different substrates

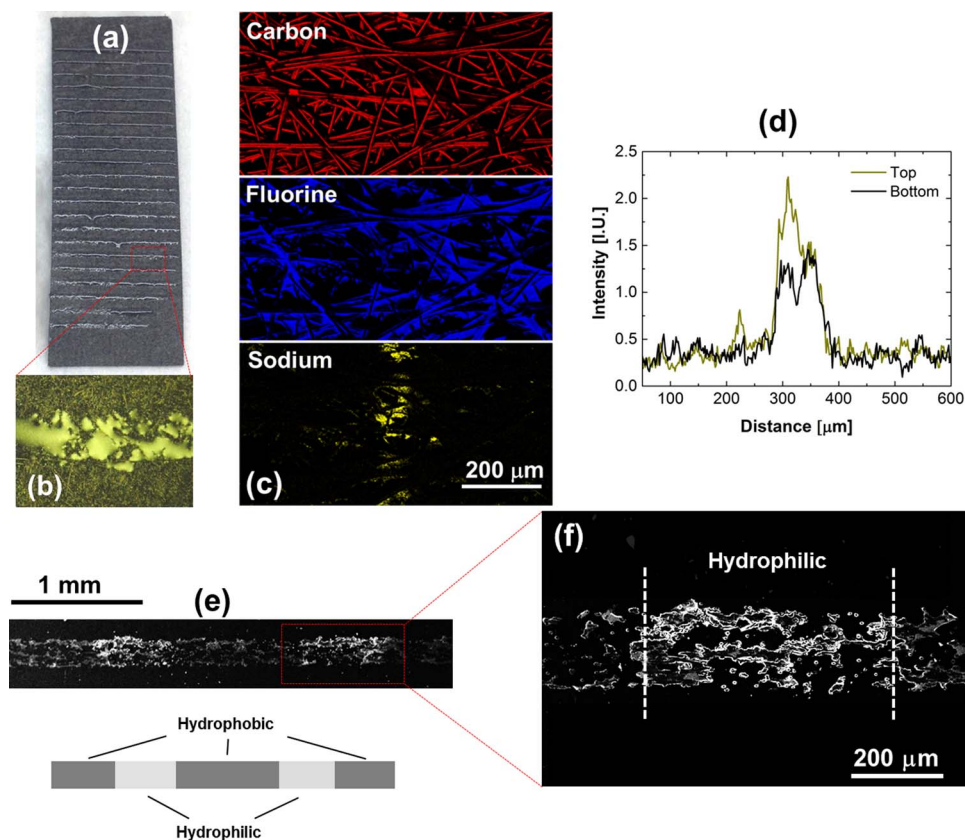


Figure 3. (a) Water accumulation in the hydrophilic patterns. Sample: Freudenberg 30%FEP-g-pNVF 500–930 μm ; (b) Closer look at the water accumulation on the hydrophilic pattern using an optical microscope; (c) EDX mapping showing the fibers (carbon signal), the coating (fluorine signal) and the grafted regions (sodium signal). Sample: Toray 70%FEP-g-pAA 100–500 μm with sodium replacement; (d) Averaged sodium intensity profile of the EDX elemental mapping of the top and bottom surfaces; (e) SEM image (secondary electrons detector) of a cross section showing two hydrophilic patterns. Sample: Toray 30%FEP-g-pAA 500–930 μm ; (f) Details of a cross section demonstrating that the coating modification occurs through the complete material thickness.

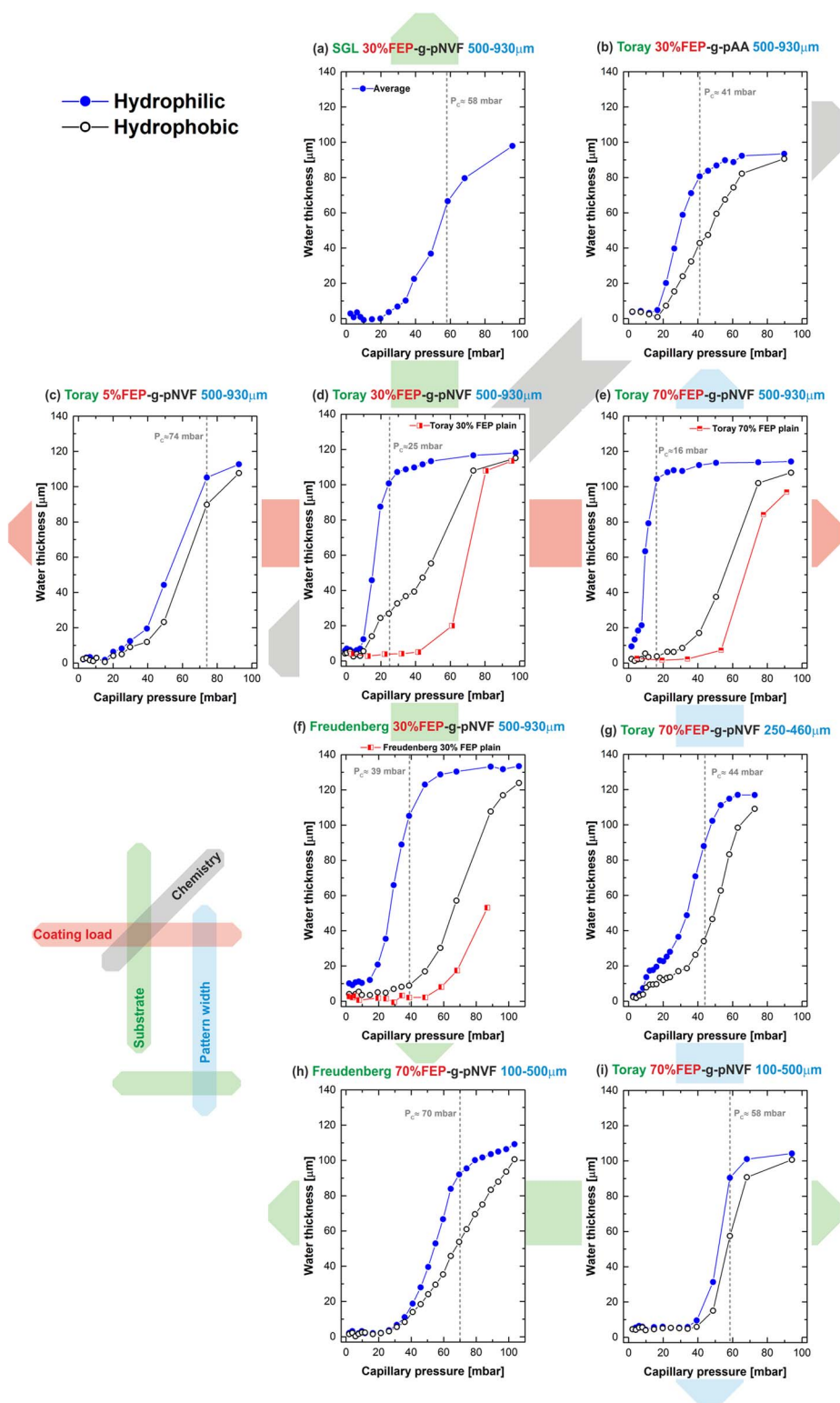


Figure 4. Water thickness versus capillary pressure curves of differently modified materials. The blue filled symbols represent hydrophilic domains while empty black symbols the hydrophobic domains. Red squares represent points of measurements on corresponding untreated samples (base-lines).

(SGL, Toray and Freudenberg) are compared. In horizontal alignment (Figures 4c, 4d and 4e) a study with three coating loads (5, 30 and 70%wt FEP) is provided. Diagonally, a comparison (Figures 4d and 4b) of the chemistry used (NVF or AA) for grafting polymerization is presented. Last, we study (Figures 4e, 4g, 4i and 4h) the influence of the hydrophilic pattern width where three patterns (500–930, 250–460 and 100–500 μm) are compared. The effect of varying the substrate (Toray and Freudenberg) is studied using the narrowest pattern as well (Figures 4i and 4a). Figure 5 is organized in the same way and

contains neutron radiographs at selected P_c (indicated in Figure 4). The impact of the parameter variations is presented and discussed in the following paragraphs.

Influence of substrate.—Figure 4d shows the P_c characteristic of a Toray 30%FEP-g-pNVF 500–930 μm. In this case, the hydrophilic domains are nearly saturated at 20–25 mbar, while water content in the hydrophobic domains remains low (Figure 4d). The P_c characteristic of the baseline material (Toray 30%FEP untreated) showed that

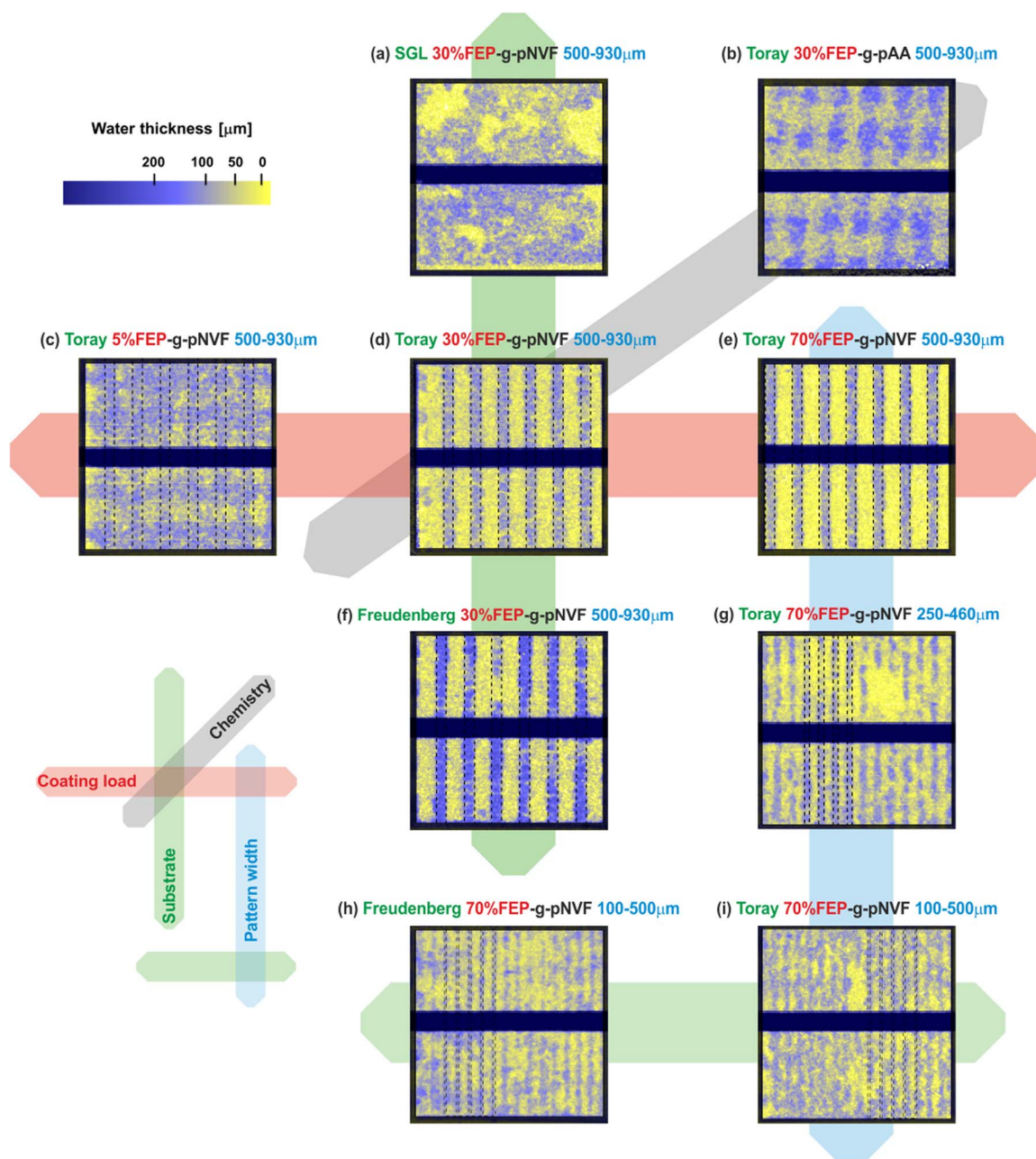


Figure 5. Neutron radiographs at selected capillary pressures (shown in Figure 4) for differently treated materials.

much higher P_C is required to fill the GDL sample (i.e. it is still nearly empty at 40 mbar), which shows the influence of the hydrophilic patterns on the hydrophobic domains. The neutron radiograph shows well-defined water filled patterns of 500 μm width (the dashed lines indicate the original line width) at 25 mbar (Figure 5d). The Freudenberg 30%FEP-g-pNVF 500–930 μm characteristic is plotted in Figure 4f. With this substrate, higher P_C is needed to fill the hydrophilic patterns (>40 mbar) while the hydrophobic domain remains almost dry. Perfectly defined water channels are observed (Figure 5f). The corresponding baseline material (Freudenberg 30%FEP untreated) also shows that higher pressure is needed to imbibe the sample with water (as compared to the hydrophobic domains of the treated sample).

The capillary pressure characteristic of SGL 30%FEP-g-pNVF 500–930 μm reveals no sign of patterned water distribution (Figure 5a); therefore only an average water thickness (for the whole sample area) is herein provided (Figure 4a).

The impossibility of forming patterns using the SGL substrate material (Figures 4a and 5a) in the capillary pressure experiment highlights the relevance of the microstructure for the water transport. Even when a high coating load was used (SGL 70%FEP-g-pNVF 250–460 μm), a very similar behavior is observed when imbibing the SGL material (Figure S2). We were able to give proof of the presence of hydrophilic patterns in the modified SGL material both by chemical mapping with EDX and by immersing the material in water and clearly observing water accumulation on the hydrophilic patterns (Section S3). However, the observation of the water distribution during imbibition suggests that water preferentially fills the larger pores, which are randomly distributed throughout the material. The location of the pores filled first does not necessarily coincide with the existing hydrophilic pattern. This observation points to the fact that large pores – even if hydrophobic – are filled at lower (or similar) pressures than small hydrophilic pores.

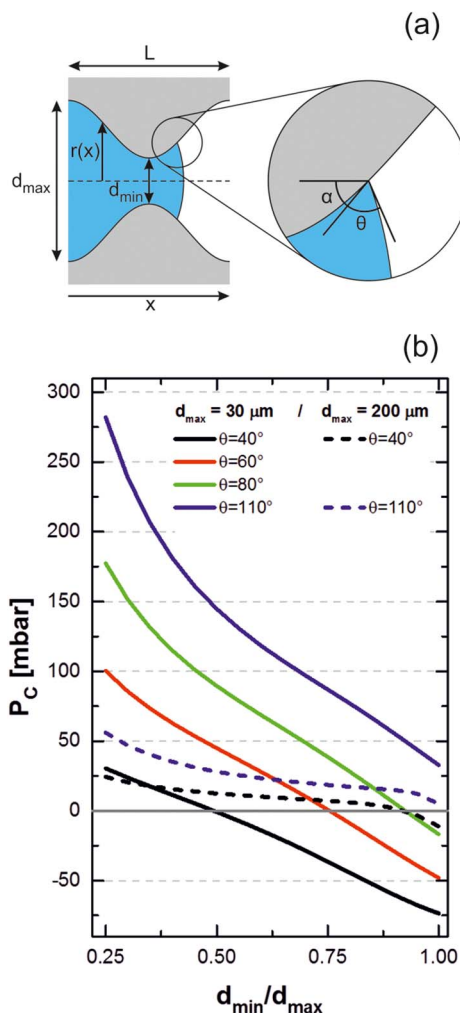


Figure 6. (a) Illustration of the geometry considered for the capillary pressure model; (b) Calculated values of capillary pressure versus d_{min}/d_{max} for different contact angles and d_{max} .

This is contradictory to the expectations if considering the Washburn equation (see Appendix), which predicts a negative capillary pressure for any hydrophilic pore and a positive capillary pressure for any hydrophobic pore. The Washburn equation is, however, derived from capillary geometries that do not feature the constrictions between pores which are typical of fibrous materials. In this paper the Young-Laplace equation is derived for a cylindrical pore with a variable constriction diameter (Figure 6a). With this approximation we do not claim to provide a fully accurate representation of an actual GDL, which is much more complex, but to include a straightforward theoretical basis to explain experimental observations that might seem counterintuitive.

P_C vs d_{min}/d_{max} curves for various contact angles and pore diameters are represented in Figure 6b. It can be seen that at a given value of d_{min}/d_{max} , the P_C dependence on contact angle is much greater for smaller pore radii. For the case of $d_{max} = 200 \mu m$, the influence of contact angle is much less significant. This could explain the reason behind the rather arbitrary water filling of SGL materials. Lamibrac et al. recently extracted pore size distribution for SGL and Toray materials using XTM data.⁴⁷ They demonstrated that SGL 24BA presents a much broader pore size distribution compared to Toray TGP-H-060. Additionally, SGL contains a notable number of rather wide pores (range of 200 μm diameter) which do not exist in the Toray or Freudenberg materials. Parikh et al. extracted pore size distribution of SGL, Toray and Freudenberg materials from scanning electron microscopy.⁵⁵ An average pore diameter of 31.8, 26.4 and

16.5 μm was obtained for SGL, Toray and Freudenberg, respectively. Freudenberg seems to present the narrowest pore size distribution, followed by Toray and finally SGL. This means that the Freudenberg substrate contains the smallest pores and that the pore size is most uniform within this series. The minimal contact angle obtained by grafting pNVF onto FEP is 20°, but we assume a higher contact angle of $\theta = 60^\circ$ for the hydrophilic pores due to the limited coverage of carbon fibers.³⁴ Similarly, we assume an internal contact angle of $\theta = 110^\circ$ for the hydrophobic pores. The results shown in Figure 6b highlight that large pores, even if hydrophobic, can be filled at a lower (or similar) pressure than hydrophilic but smaller pores (at a wide range of d_{min}/d_{max}). It should be furthermore considered that the flake-like binder, which covers a significant fraction of the carbon fibers in an SGL substrate, presents additional complications to the water transport modelling, since we have no information about the wettability of the binder surfaces with respect to the carbon fiber and/or coating, nor how the coating specifically covers each of these features.

The tendency herein observed also explains why a higher capillary pressure is required to fill the hydrophilic domains in the modified Freudenberg materials compared to those of the modified Toray GDLs (Figures 4f and 4d). Again, this is contradictory to the predictions of the Washburn equation, which would predict a negative pressure for all hydrophilic pores.

It is worth mentioning that the calculations performed herein (Figure 6) provide an approximate estimation of the penetration capillary pressure for different geometries and surface properties. Therefore, a more detailed modelling approach, such as the pore network modeling or full morphology (Lattice Boltzmann) simulations^{56–60} would bring a more realistic description of the phenomena.

Influence of coating load.—Focusing on Toray as GDL substrate, the effect of the polymeric coating load was studied (Figures 4e, 4d and 4e). When using low FEP amounts (5%wt), there is nearly no difference between the capillary pressure characteristics in hydrophobic and hydrophilic domains (Figure 4c). As previously described, the modified sample with 30%wt of FEP (Figures 4d and 5d) shows clearly defined patterns with the hydrophilic domains being nearly filled at 25 mbar. Interestingly, the increase of coating load to 70%wt slightly reduces the capillary pressure necessary to fill the hydrophilic domains (~16 mbar), while the water content in the hydrophobic regions is virtually zero for pressures below 40 mbar (Figure 4e). Thus, the water segregation into hydrophilic and hydrophobic domains is significantly more pronounced in the material with the higher coating load (Figure 5e). The probable reason for the impact of coating load is the change of coverage of the carbon fibers (Figure 7), resulting in a decreasing internal contact angle for increasing loads in the hydrophilic regions. The coexistence of surfaces with different wettability gives rise to the so-called mixed wettability.⁶¹ The contact angle of Toray (uncoated) fibers was found to be around 80°,⁶² while the contact angle of the pNVF grafted FEP is around 20°. The assumption of a decreasing contact angle (in the grafted regions) with increasing coating load is in line with the observations made in our previous work. It was proven that higher coating loads (with the very same chemical modification) led to faster wetting dynamics.³⁴ This was explained by the increase of carbon fiber surface coverage and a concomitant increase in overall (or average) hydrophilicity. A similar effect can be expected in the opposite direction for the hydrophobic regions: the contact angle should increase with the coating load, as a result of the mixed wettability between the carbon fibers (~80°) and the untreated FEP (~110°). Based on the P_C calculations for different internal contact angles (Figure 6b), the improved segregation for higher coating loads can be explained by these changes in contact angle, as the capillary pressure is generally positive except for very hydrophilic materials (e.g. 40°) and highly dependent on the effective internal contact angle.

Influence of hydrophilic pattern width.—The capillary pressure characteristic of materials with different pattern width (Figures 4e, 4g, 4i) show an interesting trend: the narrower the hydrophilic pattern,

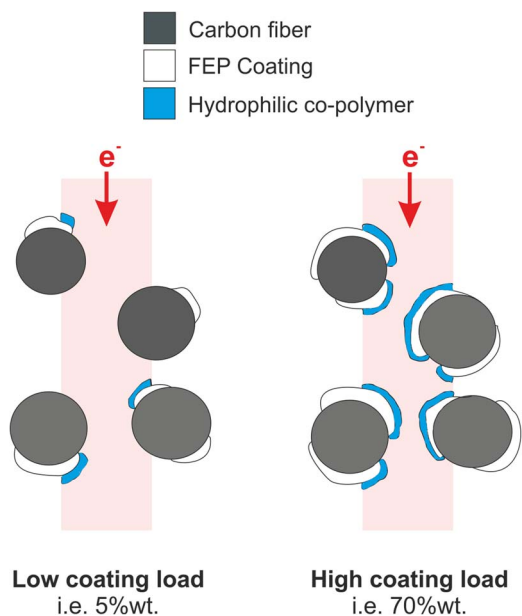


Figure 7. Illustration showing the effect of coating load on carbon fiber coverage by coating and subsequent grafting.

the higher the P_C required for imbibition of the hydrophilic regions. As a logical consequence, the separation between hydrophobic and hydrophilic domains is less defined for thin patterns (Figures 5c, 5g and 5i). For the thinnest lines (100 μm), although a faint pattern is still visible, the analysis of neutron radiographs shows that the width of the water filled region is approximately 250 μm , which is clearly larger than the grafted region. Assuming that wettability of the hydrophilic domains is the same in every case, the explanation has to be associated with microstructural details. In order to provide a water pathway, a continuous network of connected pores with reasonably large throat sizes needs to be available. The probability of providing such a network is evidently higher for wide hydrophilic domains. For thin domains, the probability increases that the pathway is obstructed by a barrier of small throats creating a bottleneck which requires a

higher capillary pressure to overcome. We further analyzed the case of 100 μm thin hydrophilic domains with another substrate (Freudenberg 70%FEP-g-pNVF 100–500 μm), with the results presented in Figures 4h and 5h. In this case, the water segregation between hydrophobic and hydrophilic domains is slightly better, which can be attributed to two reasons (Figure 8). First, the capillary pressure in the hydrophobic regions is higher due to the smaller average pore size. Second, the smaller pore size and narrower pore size distribution of this substrate reduces the probability of having a bottleneck along the water pathway.

Water distribution during evaporation.—The observation of water distribution during the removal by evaporation gives interesting further insight. In an operating cell, the phenomenon of water evaporation and condensation also plays a crucial role in the cell water balance. We observed that, when flowing dry gas through both compartments, the water occupying the hydrophobic regions is rapidly removed (in less than 2 minutes) in the case of the two modified materials (modified Toray and Freudenberg substrates with 100 μm hydrophilic patterns), while the hydrophilic patterns remain with a substantial water content for a longer time (4–6 minutes), being gradually dried. As shown in Figure 8, the water separation between hydrophilic and hydrophobic domains is much clearer during evaporation than during imbibition. These results confirm that we have well-defined hydrophilic and hydrophobic regions and support the previous explanations for the poor formation of pathways in imbibition experiments: contrary to these, evaporation does not rely on the overcoming of barrier capillary pressures. While the contact angle might only indirectly influence the evaporation rate, it is clear that the hydrophobic regions dry faster than the hydrophilic ones. For a given water volume, a water droplet in a hydrophobic domain exposes a higher surface area to the gas flow due to its curvature, therefore facilitating the evaporation process. This and the probably preferential location of water in the larger pores favor the evaporation in the hydrophobic domains first. When the water saturation is reduced, gas flow (convection) is facilitated and therefore evaporation is further favored.

Influence of grafted compound.—Another study involves the variation of the chemical treatment used for grafting. Figure 4b shows the capillary curves when acrylic acid is used as a hydrophilic monomer instead of N-vinylformamide. Compared to the latter (Figure 4d), a higher pressure is needed to fill the hydrophilic pathways (~ 40 mbar) with the filling of the hydrophobic regions following just after.

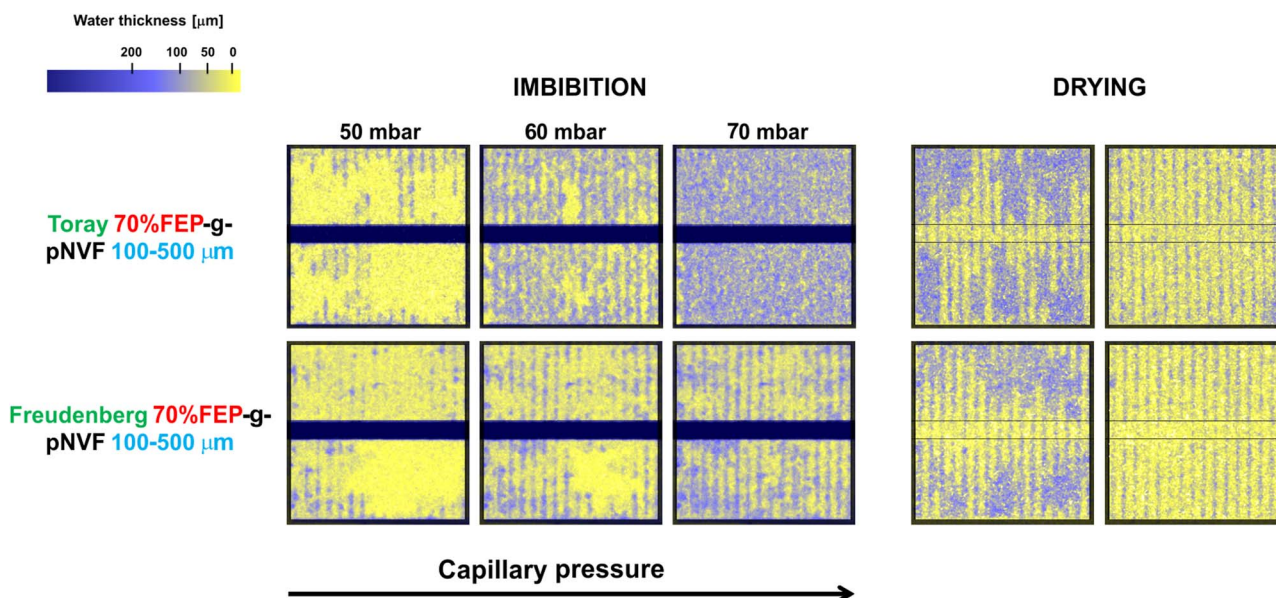


Figure 8. Neutron radiographs of imbibition (at three capillary pressures) and drying experiments of two different samples: Toray 70%FEP-g-pNVF 100–500 μm (top), Freudenberg 70%FEP-g-pNVF 100–500 μm (bottom).

Therefore, poorly defined patterns were observed in the neutron radiographs (Figure 5b). It has to be mentioned that, from the water thickness measured, we suspect that this particular sample was overcompressed ($\sim 20\%$ lower thickness), which might increase the differences due to the reduction of the pore size. Nevertheless, as the compression affects both the hydrophilic and hydrophobic regions, it cannot explain completely the differences to the base case. The effects derived from the two different chemical treatments are rather straightforward. The reason is the different intrinsic contact angles provided by the two chemistries. Measurements on flat surfaces revealed that the contact angle could be decreased from initial values of $\sim 110^\circ$ (FEP surface) to $\sim 20^\circ$ in the case of FEP-g-pNVF and $\sim 50^\circ$ for FEP-g-pAA. At a given constriction diameter (i.e. $d_{\min}/d_{\max} = 0.7$), a difference in P_C of approximately 25 mbar more is required to fill a pore grafted with acrylic acid compared to a pore treated with N-vinylformamide. These results highlight the relevance of, not only the wetting strength of the hydrophilic regions, but the ratio between both hydrophilic and hydrophobic regions' wettability in the water distribution.

Influence of the injection mode.—For one selected sample (Toray 70%FEP-g-pNVF 500–930 μm) we performed a comparative analysis using homogeneous water injection and high resolution XTM. As explained in the Experimental section, water was injected over one face of the material in this case. The separate analysis of hydrophilic and hydrophobic regions (Figure 9a) shows that already at negative capillary pressures (~ -14 mbar) the hydrophilic patterns are nearly filled. The maximum saturation is reached at about 10 mbar, while the water content in the hydrophobic regions still remains close to zero. At 20 mbar, the hydrophobic regions start imbibing and filling is completed at pressures higher than 60 mbar.

The three dimensional nature of the tomographic imaging allows a detailed analysis over the thickness of the material. Slices at three different positions (one near the injection surface, one in the middle of the sample and one near the top) at four different capillary pressures are presented in Figure 9b. The radiographs taken at -14 mbar showed that almost completely filled hydrophilic lines (of about 550 μm width) appear near the injection membrane, while the hydrophobic areas are completely water-free. A slice through the center of the GDL shows partially filled hydrophilic patterns of about 400 μm width, while the slice near the top (near the hydrophobic membrane) shows only some pores filled with water in the hydrophilic regions, which proves that breakthrough readily happens at negative capillary pressure. At 5 mbar, a width of the water-filled region of about 700 μm is measured at the bottom interface, and of 580 μm and 500 μm in the center and top slice, respectively. At increased P_C (30 mbar), the bottom interface appears nearly filled with water while significant pattern spreading occurs having wider water filled domains of about 800 and 700 μm width at the center and top slice, respectively. At higher P_C , a further broadening of the water filled regions is observed.

The differences of P_C necessary to fill the hydrophilic lines between XTM and NR experiments (-14 mbar for the homogeneous injection and $+16$ mbar for the central injection) can be explained by the anisotropy of the material,⁴⁷ resulting in important differences in the *in-plane* and *through-plane* water transport characteristics. In order to verify that they do not originate from other differences in the experimental setup, an analysis of the water distribution in the region which is in contact with the injection channel was performed (for the measurements using the NR setup). The difficulty of analyzing quantitatively the water content over the injection channel is a result of the 0.5 mm water column superimposed to the porous GDL, which significantly increases the error of the measurement. However, qualitative water distribution could be extracted (Figure 10). The differences between hydrophobic and hydrophilic regions show that the hydrophilic lines do get filled at pressures as low as 1 mbar (due to the absence of a hydrophilic membrane, negative pressures were not possible with this setup). Furthermore, the pattern widths measured at various capillary pressures match very well the measurements performed with XTM (Figure 9). Although the hydrophilic patterns under the rib appear to be filled at very low P_C , a higher pressure is required to fill the

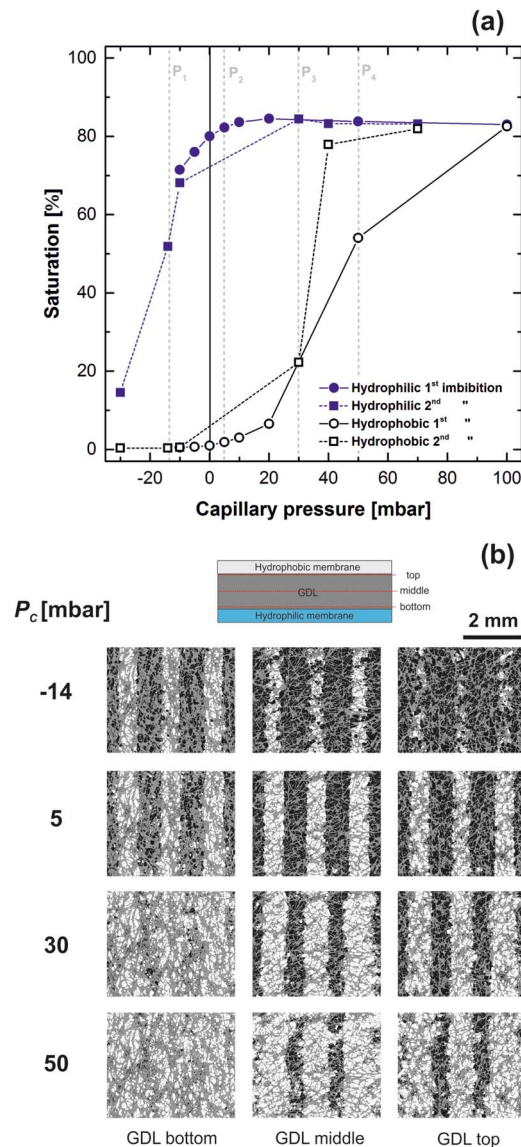


Figure 9. Capillary pressure characterization of Toray 70%FEP-g-pNVF 500–930 μm with homogeneous injection characterized with XTM. (a) Saturation versus capillary pressure curves. (b) XTM radiographs of three different slices (bottom, middle and top of the GDL sample) at four P_C (-14 , 5, 30 and 50 mbar). The irradiated side of the GDL was placed toward the injection interface (bottom).

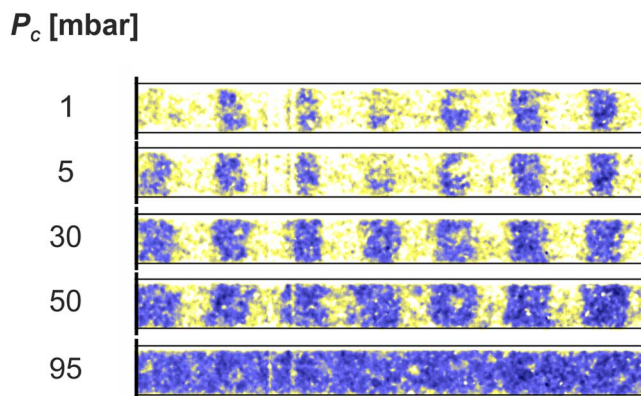


Figure 10. Neutron radiographs on the injection channel area of Toray 70%FEP-g-pNVF 500–930 μm at five different capillary pressures (1, 5, 30, 50 and 95 mbar).

adjacent areas. This result confirms that the observed differences are mainly due to the direction of injection and not to other parameters related to experimental configuration.

Implications for fuel cell operation.—The prediction of fuel cell performance from capillary pressure data (measured in such an ex situ experiment) is rather challenging. However, the results obtained shed light on two types of water transport characteristics. The mono-channel water injection forces water to travel longer distances and it is limited by the transport in lateral direction (*in-plane*), where pores are generally smaller, while the homogeneous injection setup focuses on *through-plane* transport characteristics. Both transport direction are relevant for the removal of water during fuel cell operation because, although the water is produced over the entire area, it can only be removed via the flow channels. The capillary pressure needed to fill the hydrophilic pathways is not expected to be limiting, as the electrochemical production of water can easily match the slight increase of pressure. A much more important characteristic is, at the point where the hydrophilic pathway is established, the level of water saturation in the hydrophobic regions dedicated to gas transport. Thus, the materials providing a good separation between hydrophobic and hydrophilic regions are expected to be the most suitable, even if they require higher absolute capillary pressure. According to this study, this requirement is obtained with materials having smaller pores and high coating loads. A further aspect is obviously the diffusivity of oxygen in the hydrophobic regions: even if they are not filled with water at all, the use of high coating loads might detrimentally affect this parameter. Thus, further improvements of the coating techniques to provide homogeneous coverage of the carbon fibers with a minimal amount of coating are highly desired. Nevertheless, the question of the actual fuel cell performance cannot be answered based on the ex situ characterization only. In the follow-up work (Part III of this series), in situ electrochemical characterization of operating cells combined with neutron radiography is provided and these questions are addressed.

Besides the application of our materials to reduce mass transport losses, a further possibility is to use it as a water distributor in evaporatively cooled fuel cells. In such systems, water is injected into the cell as a liquid and evaporates to remove heat.^{63,64} Using our material, an effective distribution of the liquid from injection channels over the cell area is expected.³⁰ In this case, the lateral transport is the parameter having the highest importance.

Conclusions

We have demonstrated the ability of GDLs with patterned wettability – having hydrophilic pathways dedicated to the removal of water – to confine water within the predefined pathways, although this ability heavily depends on a variety of material parameters. The main findings concerning the impact of these parameters are:

- Regular structures with low average pore size favor the patterning. While the materials based on Toray and Freudenberg substrates yield clearly defined domains, the materials based on SGL substrates – having a broad pore size distribution – show a much more random distribution of water without preferential water locations.
- Low coating loads do not permit a clear formation of water pathways.
- Narrow patterns lead to loosely defined water pathways, although the high resolution of the material modification was confirmed by SEM-EDX analysis. They also result in an increase of the capillary pressure required to fill the hydrophilic regions.
- The chemical treatment to produce hydrophilic surfaces has a major impact. Materials grafted with N-vinylformamide (providing contact angles of approximately 20°) have much better defined domains than materials treated with acrylic acid (contact angle of 50°).
- When water is injected homogeneously over one side of the GDL, the capillary pressure curves shift to lower pressure values com-

pared to the central monochannel configuration. This emphasizes the important differences in the characteristics of through-plane and in-plane water transport.

Acknowledgments

The authors gratefully acknowledge the Swiss National Science Foundation (SNSF) for funding (project numbers 143432 and 407040 153790). The Swiss Competence Center for Energy Research (SC-CER): *Efficiency in Mobility* is acknowledged for supporting this work. Dr. Thomas Yohann is gratefully thanked for preparing the GDL cross-sections. Dr. Per Magnus Kristiansen is acknowledged for providing support with the electron beam activation, Dr. Federica Marone for support at the TOMCAT beamline at the SLS, Dirk Scheuble and Martin Ammann for technical support and Ainara Irastorza for helping with the optical microscope measurements.

Appendix—Calculation of Capillary Pressure

The Young-Laplace equation relates the capillary pressure with the surface tension and mean curvature of the separating interface.⁶⁵ For cylindrical capillary tubes, the capillary pressure can be calculated as:

$$P_c = \frac{-2\gamma \cos \theta}{r}$$

where γ is the surface tension, θ the contact angle of water with the solid wall and r the pore radius. Dullien et al. considered a conical capillary.⁶⁶ We propose an extension of the cylindrical model to account for a variable constriction diameter (Figure 6a). This involves calculating a new angle, α , determined by the pore wall and the cylinder axis. If $r(x)$ is the variable pore radius, α can be calculated as:

$$\alpha = \tan^{-1} \left(\frac{dr}{dx} \right)$$

The relevant water contact angle, $(\alpha + \theta)$ can be introduced into the Washburn equation leading to:

$$P_c = \frac{-2\gamma \cos \left[\tan^{-1} \left(\frac{dr}{dx} \right) + \theta \right]}{r}$$

For a given constriction (or obstruction), we found the maximum value of $P_c(x)$. For the results presented in this paper we used a sinusoidal profile with $d_{max} = 30 \mu\text{m}$ and $L = 20 \mu\text{m}$ (Figure 6b). The value of L was chosen to have a constriction width in the range of a typical GDL carbon fiber.

References

1. R. P. O'Hayre, S.-W. Cha, W. Colella, and F. B. Prinz, *Fuel cell Fundamentals*, John Wiley & Sons New York (2006).
2. A. Rabis, P. Rodriguez, and T. J. Schmidt, *ACS Catalysis*, **2**, 864 (2012).
3. H. Li, Y. Tang, Z. Wang, Z. Shi, S. Wu, D. Song, J. Zhang, K. Fatih, J. Zhang, H. Wang, Z. Liu, R. Abouatallah, and A. Mazza, *Journal of Power Sources*, **178**, 103 (2008).
4. Y. Wang, K. S. Chen, J. Mishler, S. C. Cho, and X. C. Adroher, *Applied Energy*, **88**, 981 (2011).
5. M. F. Mathias, J. Roth, J. Fleming, and W. Lehnert, in *Handbook of Fuel Cells*, John Wiley & Sons, Ltd (2010).
6. L. Cindrella, A. M. Kannan, J. F. Lin, K. Saminathan, Y. Ho, C. W. Lin, and J. Wertz, *Journal of Power Sources*, **194**, 146 (2009).
7. S. Park, J.-W. Lee, and B. N. Popov, *International Journal of Hydrogen Energy*, **37**, 5850 (2012).
8. T. Rosén, J. Eller, J. Kang, N. I. Prasianakis, J. Mantzaras, and F. N. Büchi, *Journal of The Electrochemical Society*, **159**, F536 (2012).
9. G. S. Hwang and A. Z. Weber, *Journal of The Electrochemical Society*, **159**, F683 (2012).
10. H.-M. Chang, C.-W. Lin, M.-H. Chang, H.-R. Shiu, W.-C. Chang, and F.-H. Tsau, *Journal of Power Sources*, **196**, 3773 (2011).
11. L. Giorgi, E. Antolini, A. Pozio, and E. Passalacqua, *Electrochimica Acta*, **43**, 3675 (1998).
12. G. Lin and T. V. Nguyen, *Journal of The Electrochemical Society*, **152**, A1942 (2005).
13. G.-G. Park, Y.-J. Sohn, T.-H. Yang, Y.-G. Yoon, W.-Y. Lee, and C.-S. Kim, *Journal of Power Sources*, **131**, 182 (2004).
14. J. Biesdorf, A. Forner-Cuenca, T. J. Schmidt, and P. Boillat, *Journal of the Electrochemical Society*, **162**, F1243 (2015).
15. A. Bazylyak, D. Sinton, Z. S. Liu, and N. Djilali, *Journal of Power Sources*, **163**, 784 (2007).
16. C.-J. Tseng and S.-K. Lo, *Energy Conversion and Management*, **51**, 677 (2010).
17. M. Yoneda, M. Takimoto, and S. Koshizuka, *ECS Transactions*, **11**, 629 (2007).
18. Z. Shi, X. Wang, and O. Draper, *ECS Transactions*, **11**, 637 (2007).
19. G.-H. Yoon and Y.-i. Park, *International Journal of Precision Engineering and Manufacturing*, **13**, 1153 (2012).

20. Y. R. J. Thomas, A. Benayad, M. Schroder, A. Morin, and J. Pauchet, *ACS Applied Materials & Interfaces*, **7**, 15068 (2015).
21. T. Van Nguyen and X. Wang, US Pat. 20150024300 A1, University of Kansas (2015).
22. T. Van Nguyen, A. Aghasheini, X. Wang, V. Yarlagaadda, A. Kwong, A. Z. Weber, P. Deevanhxay, S. Tsushima, and S. Hirai, *Journal of The Electrochemical Society*, **162**, F1451 (2015).
23. F.-Y. Zhang, S. G. Advani, and A. K. Prasad, *Journal of Power Sources*, **176**, 293 (2008).
24. M. Blanco, D. P. Wilkinson, H. Wang, and S. Z. S. Liu, *ECS Transactions*, **25**, 1507 (2009).
25. D. Gerteisen, T. Heilmann, and C. Ziegler, *Journal of Power Sources*, **177**, 348 (2008).
26. E. E. Kimball, J. B. Benziger, and Y. G. Kevrekidis, *Fuel Cells*, **10**, 530 (2010).
27. M. P. Manahan, M. C. Hatzell, E. C. Kumbur, and M. M. Mench, *Journal of Power Sources*, **196**, 5573 (2011).
28. R. Koresawa and Y. Utaka, *Journal of Power Sources*, **271**, 16 (2014).
29. A. Forner-Cuenca, J. Biesdorf, L. Gubler, P. M. Kristiansen, T. J. Schmidt, and P. Boillat, *Adv Mater*, **27**, 6317 (2015).
30. P. Boillat, A. Forner-Cuenca, L. Gubler, C. Padeste, and F. N. Büchi, EP14184065.2, Paul Scherrer Institut (2014).
31. Specification Datasheet Toray Paper, <http://fuelcellsetc.com/store/DS/Toray-Paper-TGP-H-Datasheet.pdf> (Accessed 20.03.2016).
32. SGL Specifications Datasheet, http://www.fuelcellmarkets.com/content/images/articles/GDL_24_25_Series_Gas_Diffusion_Layer.pdf (Accessed 20.03.2016).
33. Freudenberg GDL Specifications Datasheet, http://www.freudenbergfuelcellproducts.com/sites/default/files/2014-12-15_technical_data_sheet_gdl.pdf (Accessed date: 20.03.2016).
34. A. Forner-Cuenca, V. Manzi-Orezzoli, J. Biesdorf, M. E. Kazzi, D. Streich, L. Gubler, T. J. Schmidt, and P. Boillat, *Journal of The Electrochemical Society*, **163**, F788 (2016).
35. A. Rafaiel, J. S. Ellis, P. R. Challa, and A. Bazylak, *Journal of Power Sources*, **201**, 219 (2012).
36. U. Pasaogullari and C. Y. Wang, *Journal of The Electrochemical Society*, **151**, A399 (2004).
37. M. M. Mench, in *Fuel Cell Engines*, p. 191, John Wiley & Sons, Inc. (2008).
38. Y. M. Volfkovich, V. S. Bagotzky, V. E. Sosenkin, and I. A. Blinov, *Colloids and Surfaces A: Physicochemical and Engineering Aspects*, **187**, 349 (2001).
39. J. T. Gostick, M. W. Fowler, M. A. Ioannidis, M. D. Pritzker, Y. M. Volfkovich, and A. Sakars, *Journal of Power Sources*, **156**, 375 (2006).
40. J. T. Gostick, M. A. Ioannidis, M. W. Fowler, and M. D. Pritzker, *Electrochemistry Communications*, **10**, 1520 (2008).
41. J. T. Gostick, M. A. Ioannidis, M. W. Fowler, and M. D. Pritzker, *Journal of Power Sources*, **194**, 433 (2009).
42. E. C. Kumbur, K. V. Sharp, and M. M. Mench, *ECS Transactions*, **11**, 683 (2007).
43. J. D. Fairweather, P. Cheung, J. St-Pierre, and D. T. Schwartz, *Electrochemistry Communications*, **9**, 2340 (2007).
44. T. V. Nguyen, G. Lin, H. Ohn, and X. Wang, *Electrochemical and Solid-State Letters*, **11**, B127 (2008).
45. M. J. Martínez, S. Shimpalee, J. W. Van Zee, and A. V. Sakars, *Journal of The Electrochemical Society*, **156**, B558 (2009).
46. Y. M. Volfkovich, V. E. Sosenkin, N. F. Nikol'skaya, and T. L. Kulova, *Russian Journal of Electrochemistry*, **44**, 278 (2011).
47. A. Lamibrac, J. Roth, M. Toulec, F. Marone, M. Stapanoni, and F. N. Büchi, *Journal of The Electrochemical Society*, **163**, F202 (2016).
48. J. T. Gostick, H. Gunterman, B. Kienitz, J. Newman, A. MacDowell, and A. Weber, *ECS Transactions*, **33**, 1407 (2010).
49. R. Flückiger, F. Marone, M. Stapanoni, A. Wokaun, and F. N. Büchi, *Electrochimica Acta*, **56**, 2254 (2011).
50. A. P. Kaestner, S. Hartmann, G. Kühne, G. Frei, C. Grünzweig, L. Josic, F. Schmid, and E. H. Lehmann, *Nuclear Instruments and Methods in Physics Research Section A: Accelerators, Spectrometers, Detectors and Associated Equipment*, **659**, 387 (2011).
51. E. H. Lehmann, G. Frei, G. Kühne, and P. Boillat, *Nuclear Instruments and Methods in Physics Research Section A: Accelerators, Spectrometers, Detectors and Associated Equipment*, **576**, 389 (2007).
52. P. Boillat, Advanced characterization of polymer electrolyte fuel cells using high resolution neutron imaging, in, Diss., Eidgenössische Technische Hochschule ETH Zürich, Nr. 18397, (2009).
53. Online database for Experimental Nuclear Reaction Data, <https://www-nds.iaea.org/exfor/exfor.htm>, (Accessed 15.01.2016).
54. E.-S. A. Hegazy, I. Ishigaki, A. Rabie, A. M. Dessouki, and J. Okamoto, *Journal of Applied Polymer Science*, **28**, 1465 (1983).
55. N. Parikh, J. S. Allen, and R. S. Yassar, *Fuel Cells*, **12**, 382 (2012).
56. P. K. Sinha and C.-Y. Wang, *Electrochimica Acta*, **52**, 7936 (2007).
57. J. T. Gostick, M. A. Ioannidis, M. W. Fowler, and M. D. Pritzker, *Journal of Power Sources*, **173**, 277 (2007).
58. L. Hao and P. Cheng, *Journal of Power Sources*, **195**, 3870 (2010).
59. A. Z. Weber, R. L. Borup, R. M. Darling, P. K. Das, T. J. Dursch, W. Gu, D. Harvey, A. Kusoglu, S. Litster, M. M. Mench, R. Mukundan, J. P. Owejan, J. G. Pharoah, M. Secanell, and I. V. Zenyuk, *Journal of The Electrochemical Society*, **161**, F1254 (2014).
60. H.-J. Vogel, J. Tölke, V. P. Schulz, M. Krafczyk, and K. Roth, *Vadose Zone Journal*, **4** (2005).
61. P. K. Sinha and C.-Y. Wang, *Chemical Engineering Science*, **63**, 1081 (2008).
62. D. Wood III and R. Borup, in *Polymer Electrolyte Fuel Cell Durability*, F. Büchi, M. Inaba, and T. Schmidt Editors, p. 159, Springer New York (2009).
63. S. G. Goebel, "Evaporative cooled fuel cell", US Pat. 6960404 B2, General Motors Corporation (2005).
64. J. S. Matcham, N. Grange, P. A. Benson, S. Baird, A. Kells, J. Cole, P. L. Adcock, P. D. Hood, and S. E. Foster, US Pat. 8609288 B2, Intelligent Energy Limited (2013).
65. T. Young, *Philosophical Transactions of the Royal Society of London*, **95**, 65 (1805).
66. F. A. L. Dullien, in *Porous Media (Second Edition)*, p. 117, Academic Press, San Diego (1992).